Check for updates

Research Article Vol. 33, No. 3 / 10 Feb 2025 / *Optics Express* 5958

Optics EXPRESS

Asymmetric directional transmission-emission based on hyperbolic metastructure covering the short-wave near-infrared region

TING-HAO ZHANG,[1] BAO-FEI WAN,[1] YU-QI ZHAO,[1] XING-ZHOU TANG,[1,2] AND HAI-FENG ZHANG[1,3]

[1] *College of Electronic and Optical Engineering & College of Flexible Electronics (Future Technology), Nanjing University of Posts and Telecommunications, Nanjing 210023, China*
[2] *xztang@njupt.edu.cn*
[3] *hanlor@163.com*

Abstract: Stealth and camouflage technology in the infrared band has been a topic of wide interest in recent years. Wave propagation direction control is an important technology to achieve electromagnetic stealth. One-dimensional photonic crystals (1D PhC) composed of isotropic and anisotropic dielectric is an approach for achieving orientation selection. Asymmetric directional transmission-emission is an important component in energy issues and heat transfer. The hyperbolic metamaterial (HMM) plate can realize asymmetric performances by combining 1D PhC with an HMM plate to achieve asymmetric directional control. Among them, an HMM plate comprises metallic silver and an isotropic dielectric. 1D PhC consists of an isotropic dielectric and a layered structure with uniaxial properties. The resulting performance is effective within 270-390 terahertz, achieving a relative bandwidth of 36.3% and coverage of short-wave near-infrared. The asymmetry is reflected in the directional absorption-emission function for electromagnetic waves incident at positive angles and the directional transmission passage for electromagnetic waves incident at negative angles. It has an extremely broad application prospect in infrared stealth, radiative cooling, thermal camouflage, and so on.

1. Introduction

Thermal radiation is electromagnetic (EM) wave radiation produced by the random movement of electrical charges [1], and the phenomenon of thermal radiation occurs whenever the temperature is above absolute zero. The energy of thermal radiation is transmitted in the form of EM waves from a high-temperature object to a low-temperature one without relying on any medium. With the continuous development of technology, thermal radiation technology has been widely used in infrared sensors [2,3], thermal illusions [4], thermal camouflage [5], and other fields. Conventional sources of thermal radiation [6], such as incandescent lamps, tend to produce continuous, omnidirectional, unpolarised light due to the thermally induced movement of molecules. This characteristic is not conducive to the control of thermal radiation and often results in energy losses in undesired wavelengths and directions [7]. In 2023, Ying *et al.* [8] directed thermal radiation from two atmospheric windows has been achieved using the Fabry–Pérot cavity and the Brewster effect but its selectivity is restricted due to the limitations of the Brewster effect in general. In the same year, Fan *et al.* [9] proposed a pixelated directional micro-emitter, which improves the directional control performance to a certain extent, however, the angular range of its control is small. It is clear that devices with directional selection functions are essential in the field of heat radiation. Short-wave near infrared region (SW-NIR) has important applications in infrared stealth technology, thermal emitters and other fields, and is an important part of the infrared band [2].

#550240 https://doi.org/10.1364/OE.550240
Journal © 2025 Received 26 Nov 2024; revised 11 Jan 2025; accepted 27 Jan 2025; published 5 Feb 2025

Angle selection (AS) is an important approach for directional control of EM waves. Shen *et al.* [10] proposed a method of AS using the Brewster effect in 2014, since then, different AS strategies have been presented. In recent years, a variety of perspective AS strategies have been raised that have shown promising applications in many areas, two of these works are extremely representative. One, by Iizuka *et al.* [11] in the same group in 2016, introduced an AS achieved using a photonic band gap [11] that is effective for both transverse electric (TE) mode and transverse magnetic (TM) one with extreme selectivity but is limited by the photonic band gap, which maintains the effect only in a narrow band. Another is the broadband AS achieved using one-dimensional (1D) photonic crystals (PhC) of isotropic and anisotropic layers brought by Qu *et al.* in 2018 [12]. This approach sacrifices some selectivity but achieves an expansion of bandwidth. In addition to these, there is a lot of excellent work in the field of AS, such as the use of Bragg reflector, gradient epsilon-near-zero materials, and uniaxial artificial dielectric-EM plates [13–16]. AS is of significant value in antenna design, privacy protection, and other areas where EM direction control is required. Overall, AS focuses on aspects of polarization, selectivity, and bandwidth, and the principles that usually fit the requirements are employed in general design.

Asymmetry has a crucial role in the design of EM devices, such as dynamic spatiotemporal modulation, optical isolators, and EM shielding [17–19]. Asymmetric devices have been extensively studied over the last few decades. The prevalent methods of realizing asymmetry are mainly achieved through the EM field response of the materials such as using weyl semimetals [20], and plasma with enhanced Faraday rotation [21]. Meanwhile, the realization of asymmetric effects using HMM is an important method of asymmetric research. Asymmetric directional control with means of metal-insulator-metal metastructure [8] and resonant gratings [22] is a typical example of the use of structural features to achieve asymmetric functionality. HMMs embody complex pattern characteristics because of their various anisotropic EM properties [23]. A flat plate made of stacked metallic multilayer film structures possess HMM properties [24] can be called HMM plate. Effective-medium theory [25] and transfer matrix method (TMM) [26] can be used to calculate the properties of HMM plate. Due to the anisotropic nature of HMM plate, it has different responses to EM waves incident at positive angles (+θs) and negative angles (-θs) [27], which can be used to achieve the effect of asymmetric control of EM waves. The introduction of HMM is a new means of achieving asymmetric performance. The structure of HMM plate is even simpler than a grating, and it is a concise and effective method of achieving asymmetric effects, which is potentially valuable in the fields of enhancement of spontaneous radiation, biosensing, and so on [28–30].

In this paper, a hyperbolic metastructure (HMS) is presented to achieve ultra-wideband asymmetric directional control. [28] HMM plate with asymmetric nature and 1D PhC structure work together to achieve the final result. HMM plate achieves an ultra-broadband angular asymmetric effect, however, its selectivity is poor. 1D PhC structure achieves broadband symmetric AS. When the EM waves under TM mode pass through the 1D PhC, only the EM waves within the selected range can be transmitted through. When the EM wave enters the HMM plate, the EM waves incident at +θs is absorbed, and the EM waves incident at -θs continues to transmit through the HMM plate. According to Kirchhoff's law [31] in thermodynamics, the absorption is equal to the emission in thermal equilibrium. The ultra-wideband asymmetric directional control device proposed in this paper forms a directional emission for positive-angle incident EM waves and a directional transmission for negative-angle incident EM waves in 270-390 terahertz (THz). It has a relative bandwidth of 36.3%, covering the entire SW-NIR. The emission from +θs can achieve the effect of radiative cooling, and the directional transmission on the negative scale can be used in thermal camouflage, infrared stealth, and other fields. The design overcomes many previous problems of thermal radiation without direction, polarization, and narrow bandwidth, and achieves excellent performance, providing a guiding method for solving problems in the field of thermal radiation.

2. Design and method

2.1. Theoretical model

The structural composition of HMM plate is shown in Fig. 1. Figure 1(a) indicates that the device is spliced by 1D PhC and HMM plate, where $d_1 = 7$ µm and $d_2 = 15$ µm. Figure 1 (b) shows the specific structure of 1D PhC, which is formed by the alternating arrangement of various isotropic and anisotropic media, where $d_A = 50$ nm, and $d_B = 50$ nm. Taking one layer of isotropic and anisotropic media as a period, the 1D PhC contains a total of the total number of periods in 1D PhC is 70. $\varepsilon_A = 2.6$, $\mu_A = 1$ [32] is the isotropic dielectric and the tensor form of the dielectric B is $\varepsilon_B = (2.49, 2.50, 2.50)$ [13], $\mu_B = 1$ is the anisotropic dielectric. The dielectric B is the result of the equalization, the construction method of a layer of anisotropic dielectric B is indicated in Fig. 1 (c). The two dielectrics B1 and B2 are arranged alternately in the surface direction. $d_{B1} = 20$ nm and $d_{B2} = 20$ nm, which are much smaller than the scale of the wavelength of incident EM wave wavelength, can be equated by the theory of equivalent media in the propagation direction and the surface direction, respectively. Figure 1 (d) shows a schematic diagram of the HMM plate, which consists of an alternating arrangement of silver (Ag) [33] and an isotropic dielectric. Where the dielectric parameter of Ag can be described by the Drude model [33], and in HMM plate $\varepsilon_C = 3.2$, $\mu_C = 1$ [34]. The structural parameters of the HMM plate are illustrated in Fig. 1 (e), where $d_C = 50$ nm, $d_{Ag} = 10$ nm, φ=30°.

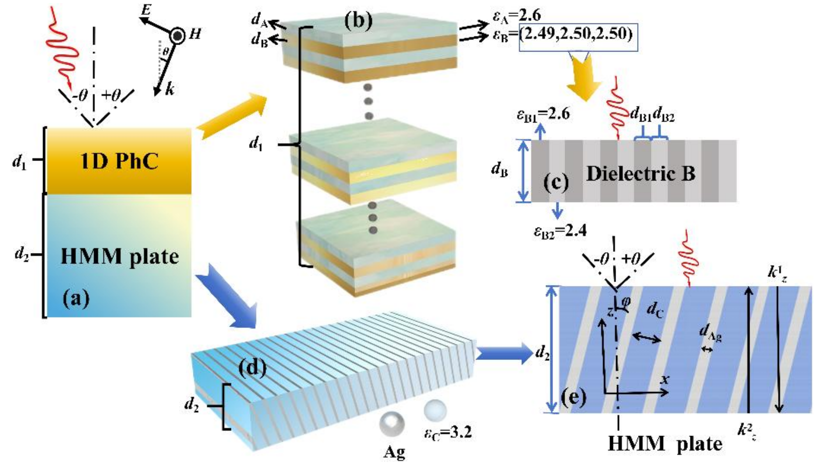

Fig. 1. (a) The overall configuration of the ultra-wideband asymmetric directional control device; (b) The specific structure of 1D PhC is composed of alternating arrangements of isotropic and anisotropic media; (c) The synthesis method of anisotropic media, where the red arrow represents the direction of incidence; (d) Three-dimensional structural diagram of HMM plate; (e) The planar structure of HMM plate is composed of Ag and isotropic dielectric, where $k^1{}_z$ and $k^2{}_z$ represent two opposite wave vectors in the propagation direction.

2.2. Calculation method

Metal has the characteristics of dielectric parameters with small real part and large imaginary part [35], and a series of phenomena such as surface plasmon which can be excited by metal [35]. In previous studies [33,35], the Drude model of metals has been verified to be correct and effective theoretically and experimentally [36]. Ag is a kind of widely used metal, and its dielectric parameters can be described as follows [33]:

$$\varepsilon_m = 1 - \frac{\omega_p^2}{\omega(\omega + i\gamma)} \tag{1}$$

In Eq. (1), $\omega_{\mathrm{p}} = 1.37 \times 10^{16}$ Hz and γ=3.21 × 10^{13} Hz. As shown in Fig. 1 (d), the Ag in the proposed metastructure is arranged alternately with each isotropic dielectric in the x-direction and tilted at 30°. The un-tilted case, i.e., each anisotropic dielectric layer in Fig. 1 (c), is considered first. When the dielectric film size is much smaller than the incident wavelength scale, in each of the two directions it can be equated with the equivalent dielectric theory [25], which eventually results in a dielectric tensor form similar to that of a uniaxial crystal [25]. The 1D arrangement of the HMM plate is illustrated in Fig. 1 (e), for which this arrangement can be obtained by doing a rotational transformation of the uniaxial crystal. The tensor form of anisotropic media layers in 1D PhC can be equivalent to [37]:

$$\widetilde{\varepsilon} = \begin{pmatrix} \varepsilon_{xx} & 0 & 0 \\ 0 & \varepsilon_{yy} & 0 \\ 0 & 0 & \varepsilon_{zz} \end{pmatrix} \tag{2}$$

Among them, ε_{xx}, ε_{yy}, and ε_{zz} represent the equivalent dielectric constants in three directions, and their values can be obtained through equivalent medium theory [34]. The dielectric constant components in each direction are: [36]:

$$\varepsilon_{yy} = \varepsilon_{zz} = \varepsilon_m f_m + \varepsilon_e f_e \tag{3}$$

$$\varepsilon_{xx} = \frac{\varepsilon_e \varepsilon_m}{\varepsilon_e f_m + \varepsilon_m f_e} \tag{4}$$

When a certain angle of rotation is made about the x-direction, the dielectric tensor form changes accordingly. When φ=30° represents the tilt angle in the + x-direction, the required angularly transformed basis vectors are of the form [38]:

$$\mathbf{P} = \begin{bmatrix} \cos\varphi & 0 & \sin\varphi \\ 0 & 1 & 0 \\ \sin\varphi & 0 & \cos\varphi \end{bmatrix} \tag{5}$$

The tensor form of HMM plate can be expressed as:

$$\widetilde{\boldsymbol{\varepsilon}} = \mathbf{p}'\widetilde{\varepsilon}\mathbf{p} = \begin{pmatrix} \varepsilon_{xx} & 0 & \varepsilon_{xz} \\ 0 & \varepsilon_{yy} & 0 \\ \varepsilon_{zx} & 0 & \varepsilon_{zz} \end{pmatrix} \tag{6}$$

where

$$\varepsilon_{xx} = \varepsilon_{xx}\cos^2\varphi + \varepsilon_{yy}\sin^2\varphi \tag{7}$$

$$\varepsilon_{xz} = \varepsilon_{zx} = (\varepsilon_{yy} - \varepsilon_{xx})\sin\varphi\cos\varphi \tag{8}$$

$$\varepsilon_{zz} = \varepsilon_{xx}\sin^2\varphi + \varepsilon_{yy}\cos^2\varphi \tag{9}$$

For isotropic dielectrics, only the effective optical admittance and spatial phase need to be calculated in the transfer matrix. For general anisotropic media such as magnetized plasma and indium antimonide [39–41], their optical rotation properties are usually considered to decompose the incident EM wave into two directions for calculation and solution. For such situations in this article, the generalized TMM is used for solving. Generally speaking, in the TMM, the two elements on the main diagonal of the phase matrix have equal absolute values [37]. In HMM plate, the upward and downward wave vectors in the z-direction are not equal and need to be changed. Firstly, the form of Maxwell's equations in the solenoidal vector region is as follows [40]:

$$\nabla \cdot \boldsymbol{D} = \rho_0 \tag{10}$$

$$\nabla \cdot \boldsymbol{B} = 0 \tag{11}$$

$$\nabla \times \boldsymbol{E} = -\frac{\partial \boldsymbol{B}}{\partial t} \tag{12}$$

$$\nabla \times \boldsymbol{H} = \frac{\partial \boldsymbol{D}}{\partial t} \tag{13}$$

In a layered structure, the magnetic field can be represented as:

$$\mathbf{H}_y = \mathbf{H}_y^+\hat{y} + \mathbf{H}_y^-\hat{y} = \mathbf{H}_{y0}^+ e^{i(k_z^+ z+k_x x-\omega t)}\hat{y} + \mathbf{H}_{y0}^- e^{i(k_z^- z+k_x x-\omega t)}\hat{y} \tag{14}$$

Among them, $k_z{}^+$ and $k_z{}^-$ represent two waves propagating in the z-direction, which can be taken into Eq. (13) to obtain:

$$\nabla \times H_y = \begin{vmatrix} \hat{x} & \hat{y} & \hat{z} \\ \frac{\partial}{\partial x} & \frac{\partial}{\partial y} & \frac{\partial}{\partial z} \\ 0 & H_y & 0 \end{vmatrix} \tag{15}$$

Similarly, from Eq. (10), it can be evolved that:

$$\begin{pmatrix} D_x \\ 0 \\ D_z \end{pmatrix} = \varepsilon_0 \begin{pmatrix} \varepsilon_{xx} & 0 & \varepsilon_{xz} \\ 0 & \varepsilon_{yy} & 0 \\ \varepsilon_{zx} & 0 & \varepsilon_{zz} \end{pmatrix} \begin{pmatrix} E_x \\ 0 \\ E_z \end{pmatrix} \tag{16}$$

$$\frac{\partial \mathbf{D}}{\partial t} = -i\omega\varepsilon_0(\varepsilon_{xx}E_x + \varepsilon_{xz}E_z)\widehat{x} - i\omega\varepsilon_0(\varepsilon_{zx}E_x + \varepsilon_{zz}E_z)\widehat{z} \tag{17}$$

From this, it is derived that:

$$\begin{cases} k_z^+ H_y^+ + k_z^- H_y^- = \omega\varepsilon_0(\varepsilon_{xx}E_x + \varepsilon_{xz}E_z) \\ k_x(H_y^+ + H_y^-) = \omega\varepsilon_0((\varepsilon_{zx}E_x + \varepsilon_{zz}E_z)) \end{cases} \tag{18}$$

From Eq. (17), E_x can be obtained:

$$E_x = \frac{\varepsilon_{zz}k_z^+ + \varepsilon_{xz}k_x}{\omega\varepsilon_0(\varepsilon_{xx}\varepsilon_{zz} - \varepsilon_{xz}^2)} H_y^+ + \frac{\varepsilon_{zz}k_z^+ + \varepsilon_{xz}k_x}{\omega\varepsilon_0(\varepsilon_{xx}\varepsilon_{zz} - \varepsilon_{xz}^2)} H_y^- \tag{19}$$

The wave vector remains unchanged in the x-direction, while there is more than one solution for the wave vector in the z direction. To calculate k_z, we can first obtain from Eq. (5):

$$\frac{\partial E_x}{\partial z} - \frac{\partial E_z}{\partial_x} = i\omega\mu_0\mu_r H_y^+ \tag{20}$$

By substituting Eqs. (19) and (20) into Eq. (18), we can obtain the quadratic equation for k_z:

$$\varepsilon_{zz}k_z^2 + (\varepsilon_{xz}k_x + k_x\varepsilon_{zx}) + \varepsilon_{xx}k_x^2 = k_0^2(\varepsilon_{xx}\varepsilon_{zz} - \varepsilon_{xz}^2) \tag{21}$$

The two solutions of k_z obtained by solving Eq. (21) are:

$$\begin{cases} k_z^1 = \left[-\varepsilon_{xz}k_x + \sqrt{(\varepsilon_{xz}^2 - \varepsilon_{zz}\varepsilon_{xx})(k_x^2 - k_0^2\varepsilon_{zz})}\right] / \varepsilon_{zz} \\ k_z^2 = \left[-\varepsilon_{xz}k_x - \sqrt{(\varepsilon_{xz}^2 - \varepsilon_{zz}\varepsilon_{xx})(k_x^2 - k_0^2\varepsilon_{zz})}\right] / \varepsilon_{zz} \end{cases} \tag{22}$$

These two solutions correspond to two characteristic modes in the plate, which are two plane waves traveling in opposite directions. In ordinary materials, the two k_z are opposite, so the structure is symmetric. However, for the current HMM plate, if k_x is not equal to 0, then the two k_z are not opposite, as shown in Fig. 2. Thus, Eq. (22) is the origin of asymmetric transmission-emission properties.

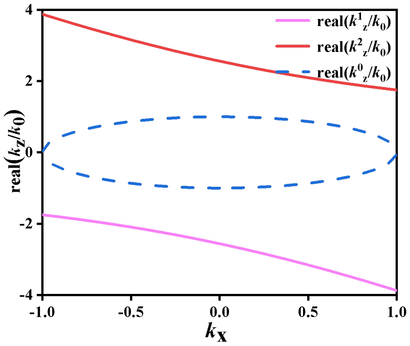

Fig. 2. The equipotential lines of HMM plate, $k^1{}_z$ and $k^2{}_z$ are two opposite wave vectors in Eq. (19), and $k^0{}_z$ represents that the equipotential line of an isotropic dielectric is a closed circle.

The configuration of 1D HMM plate is shown in Fig. 1 (d), where the metal and dielectric are alternately arranged and tilted at a certain angle. From the perspective of matrix form, the negative ε_{yy} in the tensor before tilting reflects the property of negative refraction. The tensor possesses both positive and negative refractive indices, exhibiting the characteristics of HMMs [27]. The tilted arrangement results in unequal wave vector values in the z-direction, thus distinguishing it from typical HMMs. As shown in Fig. 2, the real parts of $k^1{}_z$ and $k^2{}_z$ correspond to two hyperbolas in the iso-frequency line, respectively. When γ=0, there is no loss, and $k^0{}_z$ represents the equipotential line in this case. It can be seen that this HMM plate exhibits properties of HMMs [24].

The propagation of EM waves in HMM plate mainly occurs through the wave impedance Z, which can be expressed as [38]:

$$Z = -\frac{(k_x^2 - k_0^2\varepsilon_{zz})}{\omega\varepsilon_0(\varepsilon_{xz}^2 - \varepsilon_{xx}\varepsilon_{zz})} \tag{23}$$

The size of E_x can be represented by Z:

$$E_x = ZH_y^+ - ZH_y^- \tag{24}$$

The propagation of magnetic field at different interfaces can be obtained from the boundary conditions:

$$\begin{gathered} H_{y_i}^+ + H_{y_j}^- = H_{y_j}^+ + H_{y_i}^- \\ Z_iH_{y_i}^+ - Z_iH_{y_i}^- = Z_jH_{y_j}^+ - Z_jH_{y_j}^- \end{gathered} \tag{25}$$

Converting Eq. (25) into matrix form can be expressed as:

$$\begin{bmatrix} 1 & 1 \\ Z_i & -Z_i \end{bmatrix} \begin{bmatrix} H_{y_i}^+ \\ H_{y_i}^- \end{bmatrix} = \begin{bmatrix} 1 & 1 \\ Z_j & -Z_j \end{bmatrix} \begin{bmatrix} H_{y_j}^+ \\ H_{y_j}^- \end{bmatrix} \tag{26}$$

The matrix at the interface can be written as:

$$\boldsymbol{T} = \begin{bmatrix} 1 & 1 \\ Z & -Z \end{bmatrix} \tag{27}$$

The transfer matrix form between two interfaces can be expressed as:

$$\boldsymbol{T_i} \begin{bmatrix} H_{y_i}^+ \\ H_{y_i}^- \end{bmatrix} = \boldsymbol{T_j} \begin{bmatrix} H_{y_j}^+ \\ H_{y_j}^- \end{bmatrix} \tag{28}$$

The phase matrix in HMM plate can be expressed as:

$$\boldsymbol{P} = \begin{bmatrix} e^{-ik^2 w} & 0 \\ 0 & e^{-ik^1 w} \end{bmatrix} \tag{29}$$

The matrix at the interface between air and medium is:

$$\boldsymbol{T_1} = \begin{bmatrix} 1 & 1 \\ \sqrt{\frac{\mu_0}{\varepsilon_0}} \cos\theta & -\sqrt{\frac{\mu_0}{\varepsilon_0}} \cos\theta \end{bmatrix} \tag{30}$$

For the entire HMM plate, its total transfer matrix is:

$$\boldsymbol{M}_{HMMplate} = \boldsymbol{T}_1^{-1} \boldsymbol{T}_2 \boldsymbol{P} \boldsymbol{T}_2^{-1} \boldsymbol{T}_1 \tag{31}$$

H_{in}, H_{out}, and H_{r} denote the magnetic fields of incident, outgoing and reflected light, respectively, the following relations are satisfied:

$$\begin{bmatrix} H_{in} \\ H_r \end{bmatrix} = \boldsymbol{M_{HMM\,plate}} \begin{bmatrix} H_{out} \\ 0 \end{bmatrix} = \begin{bmatrix} M_{11} & M_{12} \\ M_{21} & M_{22} \end{bmatrix} \begin{bmatrix} H_{out} \\ 0 \end{bmatrix} \tag{32}$$

Transmission Tr, reflection R, and absorption A can be derived from the following equation:

$$\begin{gathered} Tr(\theta) = \left|\frac{H_{out}}{H_{in}}\right|^2 = \left|\frac{1}{M_{11}}\right|^2 \\ R(\theta) = \left|\frac{H_r}{H_{in}}\right|^2 = \left|\frac{M_{21}}{M_{11}}\right|^2 \\ A(\theta) = 1 - Tr(\theta) - R(\theta) \end{gathered} \tag{33}$$

The $Tr(\theta)$ in Eq. (33) indicates the transmission corresponding to the EM wave incident from $+\theta$s, and the corresponding $Tr(-\theta)$ represents the situation when incident at $-\theta$s. $R(\pm\theta)$ and $A(\pm\theta)$ are also used to distinguish EM waves incident in different directions. When dealing with anisotropic dielectric in 1D PhC, the numerical values of $\varepsilon_{\mathrm{xz}}$ and $\varepsilon_{\mathrm{zx}}$ are 0. Assigning these two values to 0 during calculation is sufficient. According to Kirchhoff's law [31], when an object is in thermal equilibrium, the directional emissivity is equal to the surface absorptivity [1]. This effect hinders energy conversion in applications. The classic method to break this situation is to use the magneto-optical effect, which essentially breaks the time reversal symmetry [42]. The tensor form of HMM plate is very similar to magneto-optical media, resulting in the asymmetric properties of HMM plate. In this case, the emissivity (e) can be calculated by the following equation: [43]:

$$e(\theta) = 1 - Tr(\theta) - R(-\theta) \tag{34}$$

The anisotropic layer and HMM plate in 1D PhC need to be calculated using equivalent methods [25]. The isotropic dielectric layer in 1D PhC can be calculated in the same form by simply degrading the TMM. Thus, the EM properties of the ultra-wideband asymmetric directional control device can be characterized by TMM. We have validated the transfer matrix method based on equivalent medium theory using HFSS, and the results show that our method is reasonable and effective.

3. Results and analysis

3.1. AS for 1D PhC

The HMS is composed of two basic units as shown in Fig. 1 (a). The red curves with arrows in Fig. 1 indicate the direction of EM wave incidence in each structure. This method of unit splicing to achieve the effect stems from the transmission nature of EM waves, which are transmitted in the 1D PhC to enter the HMM plate as an incident wave. The roles played by ID PhC and HMM plate in the HMS will be given in detail in Sections 3.1–3.3.

The Brewster effect is an important research branch in thermal radiation. For EM waves in TM mode, when θ=θ_B(Brewster angle), the EM waves are completely transmitted without reflection. The schematic diagram of this phenomenon is shown in Fig. 3.

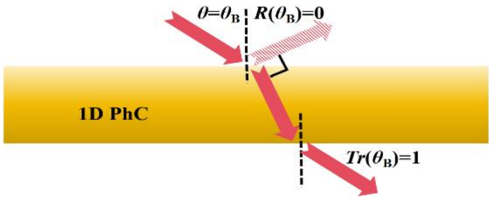

Fig. 3. Schematic diagram of Brewster effect.

In 2021, Yin *et al.* [12] constructed and experimentally verified an 1D PhC with alternating arrangements of isotropic and anisotropic media. Herein, anisotropic dielectrics are constructed, which forms the effect of ultra-wideband AS. 1D PhC consists of two dielectrics arranged periodically. When the number of 1D PhC layers (N) increases, the selectivity of the photonic band gap is enhanced for classical 1D PhC [12]. The given 1D PhC is actually a broadening of the Brewster effect. The classical Brewster effect refers to the fact that when a TM wave passes through a lossless medium, when the incident angle reaches a certain value, all the EM wave transmits through the medium [9]. This behavior can be described by the equation as [9]:

$$\theta_\mathrm{B} = \tan^{-1}\sqrt{\frac{\varepsilon_2}{\varepsilon_1}} \tag{35}$$

where ε_1 denotes the dielectric constant of the plane of incidence and ε_2 denotes the dielectric constant of the medium. In 2014, Shen *et al.* [10] firstly realized AS using the Brewster effect, however, it is only effective in a narrow band over the angular domain. The presented 1D PhC realizes the broadening of the AS region by the increase of N. As shown in Fig. 4 (a), when $N = 20$, the AS function is almost absent. As N increases, Figs. 4 (b), (c) and (d) denote the cases of $N = 40$, $N = 70$, and $N = 100$, respectively, it can be seen that as N increases, the widening of the AS region is realized with a wide band. The selection range is ±60°-80° and Tr is large in the region outside the AS region. In this paper, a novel angle-selective structure, an anisotropic dielectric plate is proposed to be constructed using a medium similar to uniaxial crystals. As shown in Fig. 1(c), the isotropic dielectric, which are arranged alternately in the $+x$-direction, have dimensions much smaller than the operating wavelength. TMM is used to obtain satisfactory AS results, as shown in Fig. 4. Due to the symmetry of the structural arrangement and the fact that the construction primitives therein are all isotropic dielectrics, the angular transmission effect is perfectly symmetric at cases of +θs and -θs in Fig. 4(d). An excellent AS effect ($Tr > 0.9$) is formed between 55°-75° with a coverage of 270-390 THz. It is instructive to the design of AS structures.

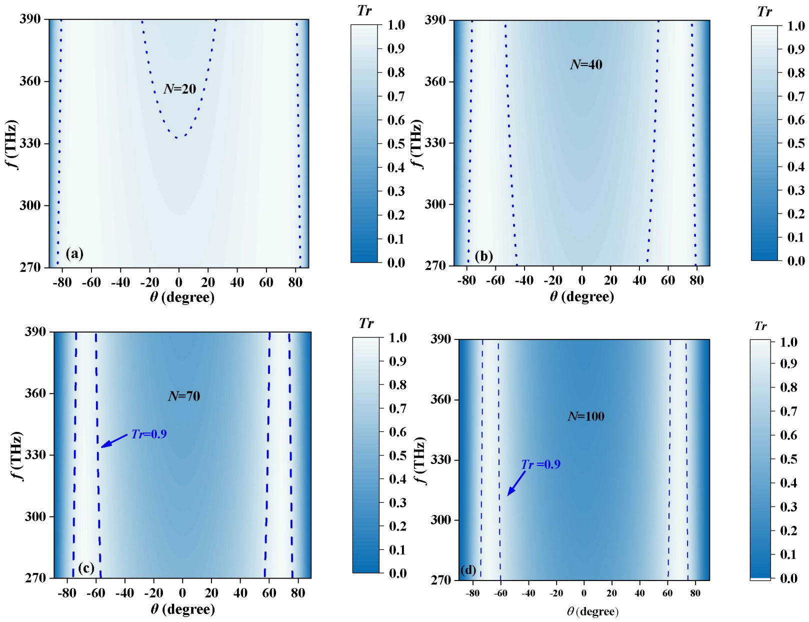

Fig. 4. Impacts of different N on AS; (a) $N = 20$; (b) $N = 40$; (c) $N = 70$; (d) $N = 100$; the AS effect of 1D PhC has the same performance in - θs and+θs, and the blue dashed line represents the area where $Tr > 0.9$.

3.2. Asymmetric transmission-emission for HMM plate

When the HMM plate in Fig. 1(c) is tilted at a 30°, the tensor form changes. Introducing a lossy medium into it can make the HMM plate have HMM properties [26]. The propagation forms of the two wave vectors in the z-direction are shown in Fig. 1(e). It can be seen from Fig. 2 that the iso-frequency lines of the z-direction wave vectors of the HMM plate are open hyperbolas, which possess the lossy condition and can form the effect of absorption. When the EM wave enters the HMM plate from -θs, it is incident under the TM mode, and the reflection is 0 when θ reaches a certain value. The transmission and absorption behavior of HMM plate at $f = 300$ THz is reflected in Fig. 5(a). The incident EM waves at +θs and -θs exhibit excellent transmission and absorption properties. And due to the significant differences among +θs and -θs, HMM plate demonstrates extraordinary asymmetric characteristics. When $\theta = \pm\theta_B$, the spectral characteristics within SW-NIR are shown in Fig. 5 (b). EM waves incident at +θs reflect good absorption performance, while those incident at -θs exhibit good transmission characteristics. To better demonstrate the asymmetric characteristics of HMM plates, three-dimensional spectral lines were drawn. Figure 5 (c) exhibits the nature of the transmission spectra, with a maximum transmission around 70°, which decreases as θ changes. This phenomenon stems from the fact that the refractive indices in the z-direction can be equated, a Brewster effect forms at the interface [9]. When the EM wave is incident from $+\theta$, HMS reflects an excellent absorption effect, as shown in Fig. 5 (d). The asymmetric Brewster effect is formed among $+\theta$s, the nature of the reflection is the same as at -θs, while the electric field of the transmitted wave is no longer perpendicular to the Ag film. Current is induced to flow along the metal surface, causing dissipation of EM waves. The HMM plate forms an ultra-broadband asymmetric absorption-transmission effect covering the near infrared wavelength band at 270-390 THz. The AS of the asymmetric transmission is alright, the dashed line for $Tr = 0.8$ remains essentially linear. However, the AS of the absorption within $+\theta$s is not good due to the limitation of the Brewster effect. From the dashed line for $A = 0.9$ the selectivity is slightly lacking within 270-390 THz. Even so, the proposed HMM plate shows great potential in ultra-wideband asymmetric effects.

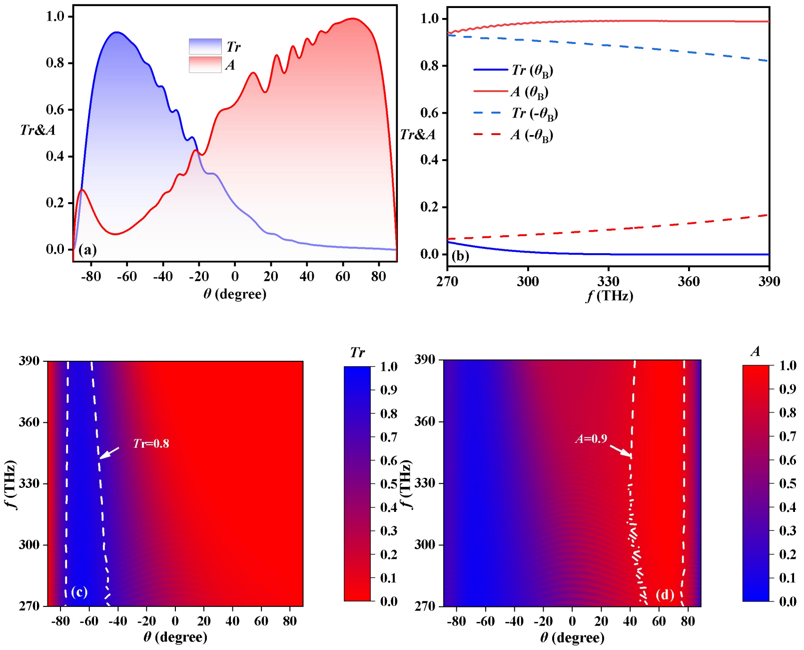

Fig. 5. Asymmetric effects of HMM plate. (a) Transmission and absorption spectra in the angular domain at $f = 300$THz and (b) in the frequency domain when $\theta=\theta_B$(c) The transmission effect of θs is divided by the white dashed line in the region where $Tr > 0.8$. (d) The absorption effect of$+\theta$s is indicated by the white dashed line, which includes the portion where $A > 0.9$.

3.3. Realization of asymmetric directional transmission-emission covering the SW-NIR

As shown in Figs. 5(a) and (b), the combination of 1D PhC and HMM plate can achieve an ultra-wideband asymmetric absorption-transmission effect. A plot of the directional transmission is illustrated in Fig. 6(a) and Fig. 5(c), where 1D PhC achieves a certain degree of selective enhancement compared to the action of HMM plate alone. The effect of directional absorption is shown in Fig. 6(b), in contrast to Fig. 5(d), the introduction of 1D PhC greatly improves the disadvantage of insufficient selectivity of HMM plate. Based on the Kirchhoff's law [31], the emissivity of the HMS can be derived as $e(\theta) = 1\text{-}Tr(+\theta)\text{-}R(-\theta)$ [43]. Since 1D PhC is symmetric in the angular domain, from Fig. 6(c), it can be seen that 1D PhC has the same reflective effect on

EM waves at +θs and -θs. According to the discussion of HMM plate in Section 3.2 and Fig. 5 asymmetric transmission-absorption is due to induced effects for EM waves in different directions of Ag. As shown in Fig. 6(d), the value of $e(\theta)$ can be derived from Eq. (34). The HMS achieves an excellent ultra-wideband asymmetric transmission-emission function covering the SW-NIR band. The directional transmission at -θs may be used in the design of thermal camouflage and infrared stealth devices. Directed emission at +θs is instructive for radiative cooling. The HMS achieves the function of ultra-wideband asymmetric directional transmission-emission, which is instructive for the design of infrared stealth devices and other radiation-related devices.

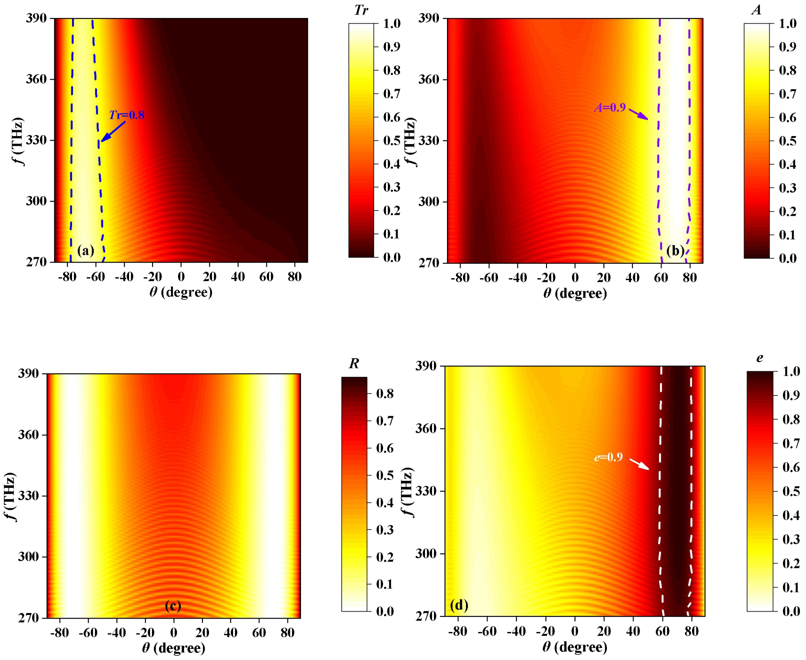

Fig. 6. The regulation of the ultra-wideband asymmetric directional control device on EM waves, (a) transmission curves, the area within the white dashed line represents the part where $Tr > 0.8$; (b) The absorption curves, with the white dashed line containing the area where $A > 0.9$; (c)The reflection spectra, indicating that+θs and -θs have almost the same reflection properties; (d) The emission spectrum line indicates that $e > 0.9$ within the white dashed line.

4. Results and analysis

4.1. Performance analysis with different metals

In this paper, Ag is selected as the absorbing material, achieving the desired effect. To illustrate the role of metals in the HMS, this section explores the influences of metal types on the absorption effect of the HMS. Metals chromium (Cr), copper (Cu), cesium (Cs), molybdenum (Mo), and tungsten (W), are selected for discussion. Dielectric constants of these metals at 300 THz are given in Table 1 [44–47], then the situations of $f = 350$ THz, $f = 270$ THz and $f = 390$ THz are shown in Tables 2, 3 and 4. Where ε’m denotes the real part of the dielectric constant, meanwhile, ε"m indicates the imaginary part. In Figs. 7(a), (b), (c) and (d), the absorption properties of different metals at 270 THz, 300 THz, 350 THz and 390 THz are plotted. In optical research, it is generally believed that the real part of the dielectric constant of metals is negative, and its absolute value increases with the redshift of spectral lines [45]. However, as the absolute value of the dielectric constant increases, the skin depth of light in the metal decreases, limiting the absorption of EM waves. Thus, metal materials should have smaller real parts and larger imaginary ones. When the metal has a small real part, the selectivity is high, and when the metal has a large imaginary part, the absorption performance is excellent. From this, suitable metals can be selected according to device requirements to achieve the desired purpose. In the given of the HMS here, as shown in Fig. 6(b), the introduction of Ag yields positive results.

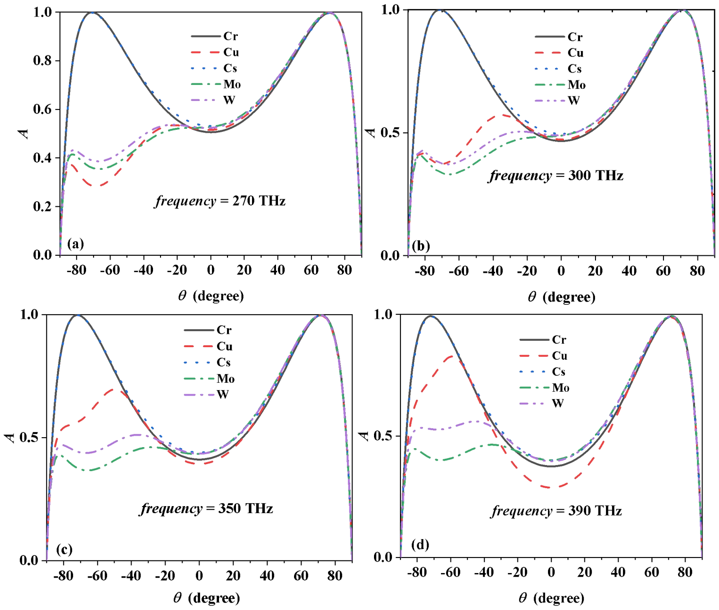

Fig. 7. Effect of different metal types on absorption performance at (a) $f = 270$ THz, (b) $f = 300$ THz, (c) $f = 350$ THz and (d) $f = 390$ THz.

Table 1. Values of real and imaginary parts of of several metals at f = 300 THz

Refs.	Metal category	ε_m'	ε_m''
[44]	Cr	-0.911	24.562
[47]	Cu	-42.704	4.266
[45]	Cs	-5.225	1.461
[46]	Mo	-194.008	107.037
[46]	W	-136.58	53.901

Table 2. Values of real and imaginary parts of of several metals at $f = 350$ THz

Refs.	Metal category	ε_m'	ε_m''
[44]	Chromium (Cr)	-1.687	22.751
[47]	Copper (Cu)	-29.886	3.065
[45]	Cesium (Cs)	-3.538	1.132
[46]	Molybdenum (Mo)	-148.56	52.801
[46]	Tungsten (W)	-98.424	27.577

Table 3. Values of real and imaginary parts of of several metals at $f = 270$ THz

Refs.	Metal category	ε'_m	ε''_m
[44]	Chromium (Cr)	0.087719	25.770
[47]	Copper (Cu)	-54.562	5.6353
[45]	Cesium (Cs)	-6.5311	1.6355
[46]	Molybdenum (Mo)	-187.08	159.28
[46]	Tungsten (W)	-145.19	80.426

Table 4. Values of real and imaginary parts of of several metals at $f = 390$ THz

Refs.	Metal category	ε'_m	ε''_m
[44]	Chromium (Cr)	-2.1454	21.300
[47]	Copper (Cu)	-22.650	2.3246
[45]	Cesium (Cs)	-2.7006	0.93620
[46]	Molybdenum (Mo)	-118.50	32.249
[46]	Tungsten (W)	-75.039	18.312

4.2. Performance analysis with φ

In the design of HMS, the φ of the HMM plate is an important parameter. φ indicates the tilt angle, which affects the behavior of EM waves in the HMM plate. The effect of different φs on the performance of HMS is plotted in Fig. 8, where the white dashed line on the left side indicates the transmission behavior for incidence at -θs and the right side indicates the absorption nature at +θs. The purple dashed lines delineate the contours of the absorption and transmission values. In Fig. 8 (a), when φ=10°, it exhibits some transmission in 270-330 THz and some absorption properties in 320-390 THz. When φ is increased, as shown in Fig. 8 (b), the bandwidth of transmission and absorption is extended at φ=20° and has some selectivity in -80°–50°, 60°-80°. In this paper, φ=30° is selected as the final value, and it can be seen from Fig. 8 (c) that the asymmetric directional control effect is good at 270-390 THz. The purple dashed lines indicate the positions of $A = 0.8$ and $Tr = 0.8$. As the angle continues to increase, the case of φ=40° is exhibited in Fig. 8 (d), and the transmission effect decreases sharply.

In the past few years, researchers have conducted extensive studies in the areas of AS, directional thermal radiation in radiative cooling and infrared stealth, and asymmetric control. However, realizing asymmetric directional control with a certain bandwidth has been a research gap. To realize the broadband effect, the effect of frequency on the material properties has to be broken. 1D PhC and HMM plate in the proposed metastructure both utilize the structural properties to realize the effect, which is beneficial for the expansion of the bandwidth. In this paper, 1D PhC and HMM plate splicing is utilized to achieve ultra-wideband asymmetric directional control. TMM is utilized for calculation, which has the advantage of simplicity and high efficiency, and experimental validation is not the core concern of this paper. The ultra-wideband asymmetric directional control is achieved by HMS in the range of 270-390 THz, and $Tr > 0.8$, e > 0.9.

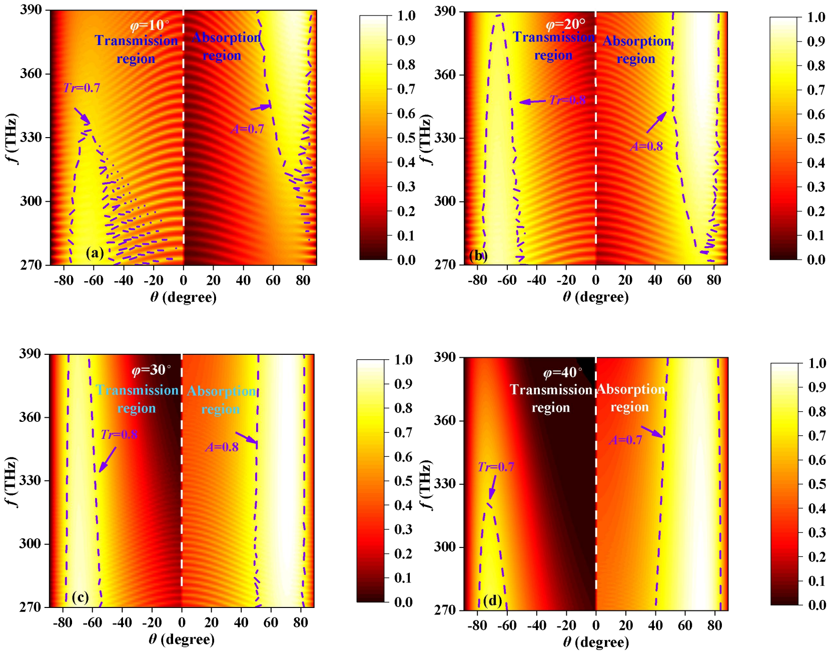

Fig. 8. Discussion of φ parameter of transmission-absorption spectral in HMM plate; (a) φ=10°; (b) φ=20°; (c) φ=30°; (d) φ=40°.

5. Conclusion

In summary, a HMS, which realizes ultra-wideband asymmetric directional transmission-emission, is proposed. Directional emission is realized in +θs and directional transmission is realized in -θs. The proposed HMS exerts its effect in 270-390 THz, covering the SW-NIR, realizing ultra-wideband characteristic. The simultaneous realization of asymmetric, ultra-wideband, and directional control in the infrared band is accomplished in the HMS. A novel approach is provided for thermal radiation-related problems. Meanwhile, the asymmetric control accomplished by HMM plate in the design can be matched to the appropriate material according to the operating band. The direction selection of EM waves is closely related to stealth and camouflage performance. It has potential value in the fields of thermal camouflage, thermal illusion, and thermal stealth.

Funding. National Key Research and Development Program of China (2022YFA1405000); National Natural Science Foundation of China (62375141); Natural Science Foundation of Jiangsu Province, Major Project, (BK20243067); National College Students Innovation and Entrepreneurship Training Program (202410293019Z).

Disclosures. The authors declare no conflicts of interest.

Data availability. Data underlying the results presented in this paper are not publicly available at this time but may be obtained from the authors upon reasonable request.

References

1. D. G. Baranov, Y. Xiao, I. A. Nechepurenko, *et al.*, "Nanophotonic engineering of far-field thermal emitters," Nat. Mater. **18**(9), 920–930 (2019).
2. W. Li and S. Fan, "Nanophotonic control of thermal radiation for energy applications [Invited]," Opt. Express **26**(12), 15995 (2018).
3. D. Rodrigo, O. Limaj, D. Janner, *et al.*, "Mid-infrared plasmonic biosensing with graphene," Science **349**(6244), 165–168 (2015).
4. R. Hu, S. Zhou, Y. Li, *et al.*, "Illusion Thermotics," Adv. Mater. **30**(22), 1707237 (2018).

5. T. Han, X. Bai, D. Gao, *et al.*, "Experimental demonstration of a bilayer thermal cloak," Phys. Rev. Lett. **112**(5), 054302 (2014).
6. O. Ilic, P. Bermel, G. Chen, *et al.*, "Tailoring high-temperature radiation and the resurrection of the incandescent source," Nat. Nanotechnol. **11**(4), 320–324 (2016).
7. J.-J. Greffet, R. Carminati, K. Joulain, *et al.*, "Coherent emission of light by thermal sources," Nature **416**(6876), 61–64 (2002).
8. Y. Ying, J. Yu, B. Qin, *et al.*, "Directional thermal emission covering two atmospheric windows," Laser Photonics Rev. **17**(11), 202300407 (2023).
9. Z. Fan, T. Hwang, S. Lin, *et al.*, "Directional thermal emission and display using pixelated non-imaging micro-optics," Nat. Commun. **15**(1), 4544 (2024).
10. Y. Shen, D. Ye, I. Čelanović, *et al.*, "Optical broadband angular selectivity," Science **343**(6178), 1499–1501 (2014).
11. H. Iizuka, N. Engheta, and S. Sugiura, "Extremely small wavevector regime in a one-dimensional photonic crystal heterostructure for angular transmission filtering," Opt. Lett. **41**(16), 3829 (2016).
12. Y. Qu, Y. Shen, K. Yin, *et al.*, "Polarization-independent optical broadband angular selectivity," ACS Photonics **5**(10), 4125–4131 (2018).
13. F. Wu, J. J. Wu, Z. W. Guo, *et al.*, "Giant enhancement of the goos-hänchen shift assisted by quasibound states in the continuum," Phys. Rev. Appl. **12**(1), 014028 (2019).
14. L. Grineviciute, C. Babayigit, D. Gailevičius, *et al.*, "Angular filtering by Bragg photonic microstructures fabricated by physical vapour deposition," Appl. Surf. Sci. **481**, 353–359 (2019).
15. J. Xu, J. Mandal, and A. P. Raman, "Broadband directional control of thermal emission," Science **372**(6540), 393–397 (2021).
16. H. Huang and Z. Shen, "Angle-selective surface based on uniaxial dielectric-magnetic slab," Antennas Wirel. Propag. Lett. **19**(12), 2457–2461 (2020).
17. K. Fang, Z. Yu, and S. Fan, "Photonic Aharonov-Bohm effect based on dynamic modulation," Phys. Rev. Lett. **108**(15), 153901 (2012).
18. L. Bi, J. Hu, P. Jiang, *et al.*, "On-chip optical isolation in monolithically integrated non-reciprocal optical resonators," Nat. Photonics **5**(12), 758–762 (2011).
19. Z. R. Zhang, H. Q. Li, H. Chen, *et al.*, "Coherent perfect absorption in one-dimensional photonic crystal with a PT-symmetric defect," Europhys. Lett. **105**(4), 47008 (2014).
20. B. Zhao, C. Guo, Christina, *et al.*, "Axion-field-enabled nonreciprocal thermal radiation in weyl semimetals," Nano Lett. **20**(3), 1923–1927 (2020).
21. M. Camacho, B. Edwards, and N. Engheta, "Achieving asymmetry and trapping in diffusion with spatiotemporal metamaterials," Nat. Commun. **11**(1), 3733 (2020).
22. K. Ito, T. Matsui, and H. Iizuka, "Thermal emission control by evanescent wave coupling between guided mode of resonant grating and surface phonon polariton on silicon carbide plate," Appl. Phys. Lett. **104**(5), 4864401 (2014).
23. G. W. Ebrahim Forati, A. B. Hanson, Yakovlev, *et al.*, "Planar hyperlens based on a modulated graphene monolayer," Phys. Rev. B **89**(8), 081410 (2014).
24. F. Wu, G. Lu, C. Xue, *et al.*, "Experimental demonstration of angle-independent gaps in one-dimensional photonic crystals containing layered hyperbolic metamaterials and dielectrics at visible wavelengths," Appl. Phys. Lett. **112**(4), 041902 (2018).
25. D. E. Aspnes, "Local-field effects and effective-medium theory: A microscopic perspective," Am. J. Phys. **50**(8), 704–709 (1982).
26. B. Wood, J. B. Pendry, and D. P. Tsai, "Directed subwavelength imaging using a layered metal-dielectric system," Phys. Rev. B **74**(11), 115116 (2006).
27. I. S. Nefedov and L. A. Melnikov, "Super-Planckian far-zone thermal emission from asymmetric hyperbolic metamaterials," Appl. Phys. Lett. **105**(16), 4899126 (2014).
28. J. Yu, R. Qin, Y. Ying, *et al.*, "Asymmetric directional control of thermal emission," Adv. Mater. **35**(45), 202302478 (2023).
29. Z. X. Li, H. L. Li, Z. D. Hu, *et al.*, "Lithography-free high sensitivity perfect absorption based on Graphene/α-MoO3/SiC and Tamm plasmonic structure," Opt. Laser Technol. **169**, 110125 (2024).
30. J. J. Zhang, Y. H. Ruan, Z. D. Hu, *et al.*, "An enhanced high Q-factor resonance of quasi-bound states in the continuum with all-dielectric metasurface based on multilayer film structures," IEEE Sens. J. **23**(3), 2070–2075 (2023).
31. L. A. Remer, E. Mohler, W. Grill, *et al.*, "Nonreciprocity in the optical reflection of magnetoplasmas," Phys. Rev. **30**(6), 3277–3282 (1984).
32. J. W. Fleming, "Dispersion in GeO_2–SiO_2 glasses," Appl. Opt. **23**(24), 4486 (1984).
33. H. Yang, J. D'Archangel, M. L. Sundheimer, *et al.*, "Optical dielectric function of silver," Phys. Rev. B **91**(23), 235137 (2015).
34. K. Kato and E. Takaoka, "Sellmeier and thermo-optic dispersion formulas for KTP," Appl. Opt. **41**(24), 5040 (2002).
35. N. Fang, H. Lee, C. Sun, *et al.*, "Sub-diffraction-limited optical imaging with a silver superlens," Science **308**(5721), 534–537 (2005).
36. D. D. Nguyen and S. Zhao, "A new high order dispersive FDTD method for Drude material with complex interfaces," Journal of Computational and Applied Mathematics **285**, 1–14 (2015).

37. H. Y. Dong, J. Wang, and T. J. Cui, "One-way Tamm plasmon polaritons at the interface between magnetophotonic crystals and conducting metal oxides," Phys. Rev. B **87**(4), 045406 (2013).
38. Y. Fang and Y. Zhang, "Perfect nonreciprocal absorption based on metamaterial slab," Plasmonics **13**(2), 661–667 (2018).
39. B. Hu, Q. J. Wang, and Y. Zhang, "Broadly tunable one-way terahertz plasmonic waveguide based on nonreciprocal surface magneto plasmons," Opt. Lett. **37**(11), 1895 (2012).
40. J. B. Pendry and A. MacKinnon, "Calculation of photon dispersion relations," Phys. Rev. Lett. **69**(19), 2772–2775 (1992).
41. A. Poddubny, I. Iorsh, P. Belov, *et al.*, "Hyperbolic metamaterials," Nat. Photonics **7**(12), 948–957 (2013).
42. W.-K. Li and G. Guo, "First-principles study on magneto-optical effects in the ferromagnetic semiconductors Y3Fe5O12 and Bi3Fe5O12," Phys. Rev. **103**(1), 014439 (2021).
43. J. Wu and Y. M. Qing, "Tunable near-perfect nonreciprocal radiation with Weyl semimetal and graphene," Phys. Chem. Chem. Phys. **25**(13), 9586–9591 (2023).
44. P. Johnson and R. Christy, "Optical constants of transition metals: Ti, V, Cr, Mn, Fe, Co, Ni, and Pd," Phys. Rev. B **9**(12), 5056–5070 (1974).
45. N. V. Smith, "Optical Constants of Rubidium and Cesium from 0.5 to 4.0 eV," Phys. Rev. B **2**(8), 2840–2848 (1970).
46. W. S. M. Werner, K. Glantschnig, and C. Ambrosch-Draxl, "Optical constants and inelastic electron-scattering data for 17 elemental metals," J. Phys. Chem. Ref. Data **38**(4), 1013–1092 (2009).
47. P. B. Johnson and R. W. Christy, "Optical constants of the noble metals," Phys. Rev. B **6**(12), 4370–4379 (1972).